Metal–Oleate Complex-Derived Bimetallic Oxides Nanoparticles Encapsulated in 3D Graphene Networks as Anodes for Efficient Lithium Storage with Pseudocapacitance

Yingying Cao[1], Kaiming Geng[1], Hongbo Geng[2] ✉, Huixiang Ang[3], Jie Pei[1], Yayuan Liu[1], Xueqin Cao[1], Junwei Zheng[4], Hongwei Gu[1] ✉

Yingying Cao and Kaiming Geng contributed equally to this work.

✉ Hongbo Geng, hbgeng@gdut.edu.cn; Hongwei Gu, hongwei@suda.edu.cn

[1] Key Laboratory of Organic Synthesis of Jiangsu Province, College of Chemistry, Chemical Engineering and Materials Science and Collaborative Innovation Center of Suzhou Nano Science and Technology, Soochow University, Suzhou 215123, People's Republic of China

[2] School of Chemical Engineering and Light Industry, Guangdong University of Technology, Guangzhou 510006, People's Republic of China

[3] School of Chemical and Biomedical Engineering, Nanyang Technological University, Singapore 637459, Singapore

[4] College of Physics, Optoelectronic and Energy, Soochow University, Suzhou 215006, People's Republic of China

HIGHLIGHTS

- Bimetallic oxides nanoparticles derived from metal–oleate complexes embedded in 3D graphene networks were fabricated by a facile and rational design approach.

- The unique porous architecture promotes charge transfer so as to enhance the reversible capacity.

- The synergetic effect between the 0D nanoparticles and 3D graphene networks plays an essential role in the superb electrochemical performance.

ABSTRACT In this manuscript, we have demonstrated the delicate design and synthesis of bimetallic oxides nanoparticles derived from metal–oleate complex embedded in 3D graphene networks ($MnO/CoMn_2O_4 \subset GN$), as an anode material for lithium ion batteries. The novel synthesis of the $MnO/CoMn_2O_4 \subset GN$ consists of thermal decomposition of metal–oleate complex containing cobalt and manganese metals and oleate ligand, forming bimetallic oxides nanoparticles, followed by a self-assembly route with reduced graphene oxides. The $MnO/CoMn_2O_4 \subset GN$ composite, with a unique architecture of bimetallic oxides nanoparticles encapsulated in 3D graphene networks, rationally integrates several benefits including shortening the diffusion path of Li^+ ions, improving electrical conductivity and mitigating volume variation during cycling. Studies show that the electrochemical reaction processes of

$MnO/CoMn_2O_4 \subset GN$ electrodes are dominated by the pseudocapacitive behavior, leading to fast Li^+ charge/discharge reactions. As a result, the $MnO/CoMn_2O_4 \subset GN$ manifests high initial specific capacity, stable cycling performance, and excellent rate capability.
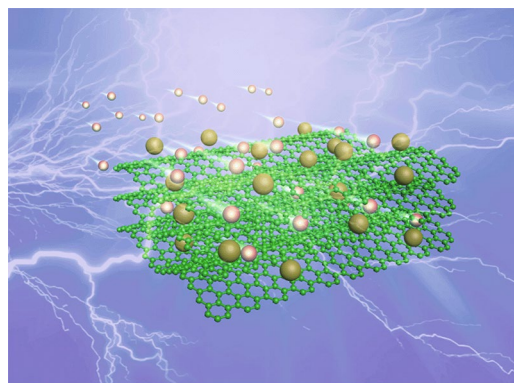
KEYWORDS Metal–oleate complex; Bimetallic oxides nanoparticles; Porous architecture; 3D graphene networks; Lithium ion batteries

1 Introduction

In recent years, there has been enormous interest for lithium ion batteries (LIBs) due to their significant merits such as small volume, long cycle life, high specific capacity, and good safety [1–3], which are applicable in various fields such as digital products, satellites, and portable mobile tools [4–7]. Compared to the traditional anode material (graphite has a low specific capacity of 372 mAh g^{-1}) [8–10], transition metal oxides (TMOs) can deliver a higher theoretical specific capacity (500–1000 mAh g^{-1}) that is promising to replace the conventional graphite material in LIBs [11, 12].

Among the examined TMO materials, cobalt oxide has attracted considerable attention for its high specific capacity of 890 mAh g^{-1} [13–15]. However, the structure variation caused by volume expansion during Li$^+$ insertion and extraction processes hinders its practical application [16–18]. As is well known, the addition of manganese into cobalt oxide structure to form cobalt–manganese binary oxides could enrich the overall valence electrons of the hybrid material, leading to enhanced electrical conductivity of the anode and thus, improve the electrochemical performance of the LIBs [19]. In addition to that, manganese in its oxide form not only possesses an extremely low operating voltage [20–22], but is also a plentiful and low-cost material which is beneficial for practical implementation [23, 24]. Interestingly, bimetallic oxides, such as CoMn$_2$O$_4$ [25], MnCo$_2$O$_4$ [26], ZnCo$_2$O$_4$ [27], ZnFe$_2$O$_4$ [28], exhibit excellent electrochemical performance owing to their complementarity and synergetic effect during the charge and discharge processes. In addition, graphene is one of the most promising templates used for supporting nanoparticles for application in LIBs [29, 30]. The dispersion of metal oxides nanoparticles on graphene-based materials could enhance the electrical conductivity and buffer volume variation of the electrode and could further improve the electrochemical performance of LIBs [31]. For instance, Yang et al. [32] presented a facile strategy for the synthesis of graphene-coated Co$_3$O$_4$ fiber electrode, which exhibits excellent cyclic stability and good rate capacity. Wang et al. [33] prepared graphene-coated Mn$_3$O$_4$ with unprecedented rate capability and cycling stability, which was attributed to the intimate interaction between graphene substrates and Mn$_3$O$_4$ nanoparticles.

Herein, we present a facile and rational design approach to fabricate MnO/CoMn$_2$O$_4$⊂GN composite, in which the MnO/CoMn$_2$O$_4$ nanoparticles are uniformly wrapped by graphene sheets, which are connected into a three-dimensional (3D) conductive network. The electrochemical performance of the as-prepared MnO/CoMn$_2$O$_4$⊂GN electrode was evaluated in LIBs, which exhibits excellent electrochemical performance, such as stable cycling performance (about 921 mAh g^{-1} over 150 cycles at 0.1 A g^{-1}) and good rate capability (about 515 mAh g^{-1} at 5 A g^{-1}).

2 Experimental

2.1 Synthesis of the CoMn$_2$O$_4$ Nanoparticles

In a typical procedure, CoCl$_2$·6H$_2$O (3 mM, 0.7138 g), MnCl$_2$·4H$_2$O (9 mM, 1.7811 g), and sodium oleate (24 mM, 7.3068 g) were dissolved in a mixture which contained 18 mL of water, 24 mL of ethanol and 42 mL of hexane, and then stirred at 70 °C for 4 h. The organic layer was separated with a separatory funnel and washed three times with water. Afterward, the as-obtained precursor was dried at 80 °C for 12 h under vacuum conditions. To synthesize CoMn$_2$O$_4$ nanoparticles, the precursor was calcined at 350 °C under Ar atmosphere for 1 h and then heated up to 600 °C in air for 3 h.

2.2 Synthesis of the MnO/CoMn$_2$O$_4$⊂GN Nanocomposite

The as-prepared CoMn$_2$O$_4$ nanoparticles (80 mg) were dispersed in 25 mL of deionized water via ultrasonication for 30 min. A modified Hummer's method was used to synthesize graphene oxide (GO) from natural graphite powder. Then, the as-obtained GO suspension was further sonicated for several hours to exfoliate the graphene oxide layers which were then dispersed in water at a concentration of 2 mg mL^{-1} [34]. Next, GO aqueous solution (40 mg, 2 mg mL^{-1}) was added into the above suspension and stirred for 6 h. The mixture was transferred and sealed in a Teflon-lined stainless steel autoclave, while keeping the reaction temperature at 180 °C for 12 h. After cooling down to the room temperature, the resulting product was washed with ethanol and water three times and then sintered at 500 °C under Ar atmosphere for 2 h. Comparable samples were prepared by a similar procedure with different feed ratios displayed in Table S1. As we can see, the sample with the higher content of Mn/GO is denoted as M1/G1, and the sample with the lower content of Mn/GO is denoted as M2/G2.

2.3 Materials Characterization

The morphology of the product was examined by scanning electron microscopy (SEM, Hitachi S-4700), transmission electron microscopy (TEM, Tecnai G220, FEI), and high-resolution TEM (HRTEM, Tecnai G2 F20 S-TWIN). The elemental constituents were characterized by energy-dispersive X-ray spectroscopy (EDS, Hitachi S-4700). The crystallographic information was analyzed by X-ray diffraction (XRD) on a X'Pert-Pro MPD diffractometer (PANalytical, Netherlands) with a Cu Kα X-ray source ($\lambda = 1.540598$ Å). Thermogravimetric analysis (TGA) was performed on PerkinElmer TGA 4000 thermogravimetric analyzer, and X-ray photoelectron spectroscopy (XPS, Escalab250Xi, UK) was conducted with a hemispherical electron energy analyzer. The specific surface area was performed via a Brunauer–Emmett–Teller (BET, Micromeritics ASAP 2020 M) analyzer, and the pore size distribution was calculated through the Barrett–Joyner–Halenda (BJH) method.

2.4 Electrochemical Measurement

The electrochemical performances of the products were measured using a coin-type half cell (CR 2016). Active materials (MnO/CoMn$_2$O$_4 \subset$ GN, 70 wt%), acetylene black (20 wt%), and polyvinylidene difluoride (PVDF, 10 wt%) were dissolved in N-methyl-2-pyrrolidone (NMP) to form a uniform slurry. Then, the slurry was spread on the copper foil as the working electrode and dried in a vacuum oven at 85 °C overnight. The mass loading was around 1.4 mg cm^{-2} on each current collector. The electrode sheets were then pressed under a force of approximately 10 MPa and cut into circular sheets. A cell was assembled in an argon-filled glove box with a lithium foil as the reference electrode, copper foil with dried anode materials as the working electrode, while a Celgard 2400 membrane served as the separator immersed in the electrolyte containing 1 M LiPF$_6$ in a mixed solution of ethylene carbonate (EC) and diethyl carbonate (DEC) with a volume ratio of 1:1. A LAND CT2001 test system was employed to perform the electrochemical measurements. The cyclic voltammetry (CV) test was carried out at a sweep rate of 0.1 mV s^{-1} with a voltage window of 0.01–3.0 V.

3 Results and Discussion

The multistep fabrication procedure of the MnO/CoMn$_2$O$_4 \subset$ GN is schematically illustrated in Scheme 1. The CoMn$_2$O$_4$ nanoparticles are obtained after thermal decomposition of the metal–oleate precursors, which were
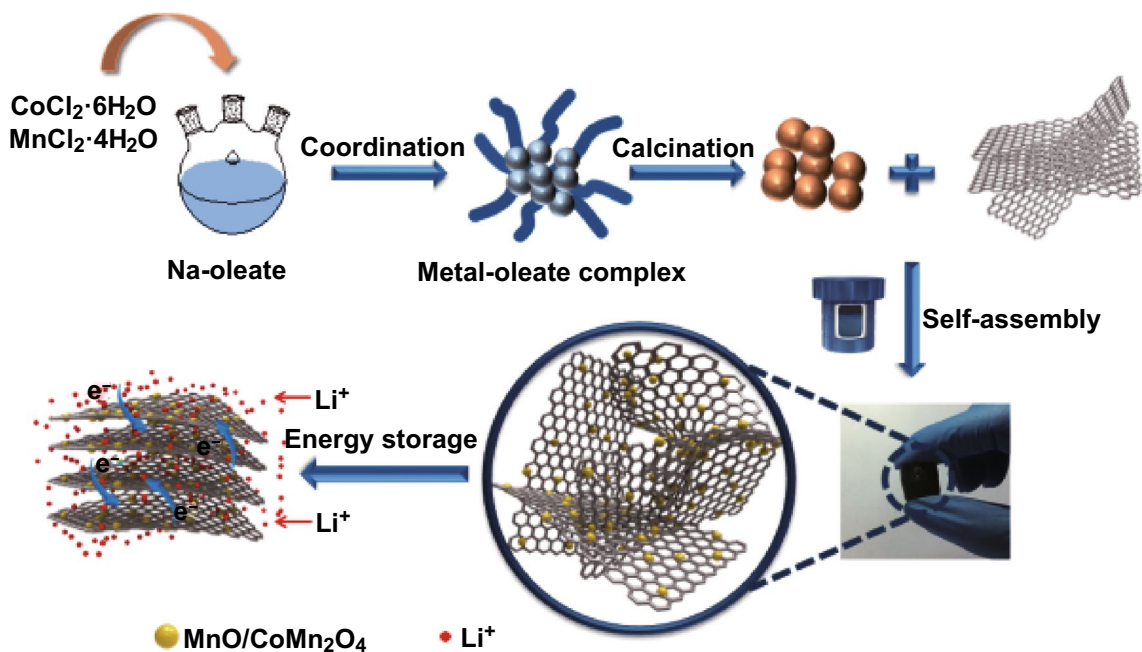
Scheme 1 Schematic illustration of the synthetic processes for MnO/CoMn$_2$O$_4 \subset$ GN

prepared by reacting $CoCl_2 \cdot 6H_2O$, $MnCl_2 \cdot 4H_2O$ and sodium oleate in mixed solvents at 70 °C for 4 h, stirring overnight and spin drying. Subsequently, the as-prepared $CoMn_2O_4$ nanoparticles were assembled with graphene sheets by a hydrothermal process and post-heat treatment, yielding $MnO/CoMn_2O_4 \subset GN$ composite.

The morphologies and structures of the $CoMn_2O_4$ sample were investigated by SEM and TEM. The SEM (Fig. 1a, b) and TEM (Fig. 1c, d) images reveal that the cobalt–manganese bimetallic oxides are composed of nanoparticles with diameters ranging from 50 to 100 nm. The optimal calcination temperature to form $CoMn_2O_4$ was determined based on the TGA (Fig. S1), performed at a temperature range from 25 to 800 °C with a heating rate of 10 °C min^{-1} under N_2 and air atmosphere. The weight loss between 10 and 350 °C under N_2 (red) might be ascribed to the removal of adsorbed water. The decomposition temperature of metal–oleate is about 500 °C under air atmosphere (black). The existence

and contents of the elements in the as-synthesized $CoMn_2O_4$ nanoparticles can be characterized by EDS (Fig. S3a and Table S2).

The $MnO/CoMn_2O_4 \subset GN$ was obtained by embedding $CoMn_2O_4$ in 3D graphene networks through a self-assembly method. As shown in Fig. 2a, b, the $MnO/CoMn_2O_4$ nanoparticles are uniformly wrapped by rough and irregular graphene networks. Further, TEM investigations reveal that almost all 0D nanoparticles are coated with graphene sheets which are connected into 3D graphene networks (Fig. 2c, d). The existence of 3D graphene networks is also confirmed by Raman spectra in Fig. S2. The G band is a characteristic feature of graphitic layers, while the D band corresponds to disordered carbon or defective graphitic structures. The intensity ratio of the D and G peak is widely used as a metric of disorder in graphene [35]. Thus, the high I_D/I_G in $MnO/CoMn_2O_4 \subset GN$ (1.13) demonstrates a more disordered structure compared to reduced graphene oxide
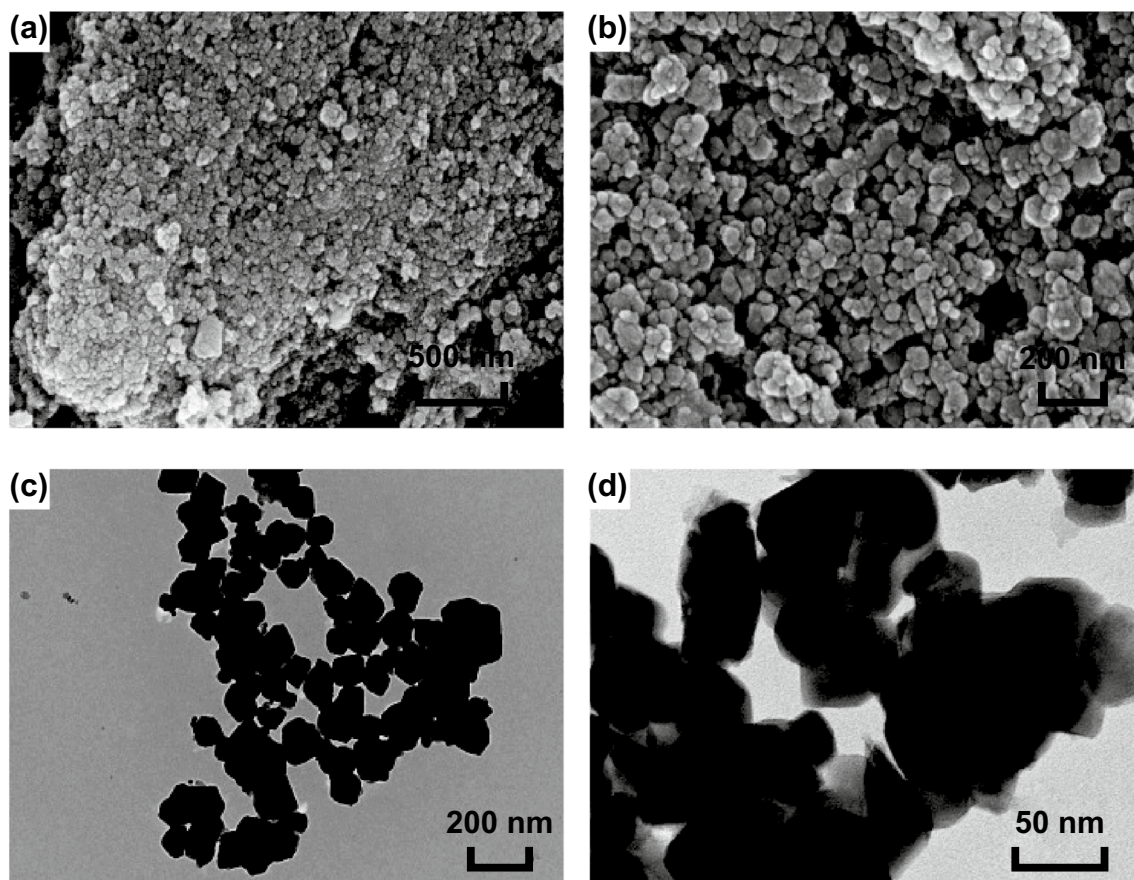
Fig. 1 **a**, **b** SEM and **c**, **d** TEM images of the $CoMn_2O_4$
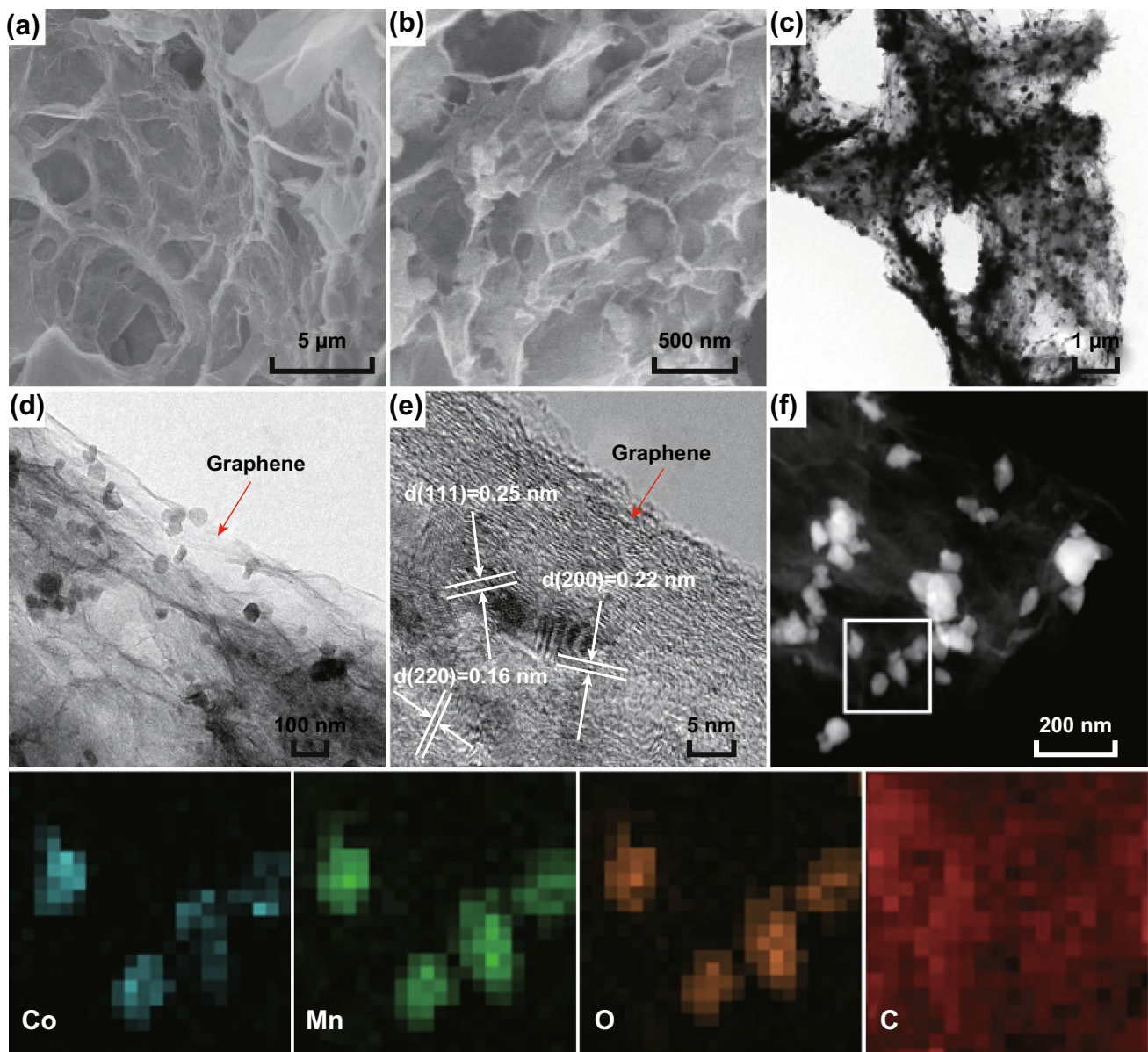
Fig. 2 **a**, **b** SEM and **c**, **d** TEM images of MnO/CoMn$_2$O$_4$⊂GN. **e** High-magnification TEM image of MnO/CoMn$_2$O$_4$⊂GN. **f** The corresponding elemental mapping images of the MnO/CoMn$_2$O$_4$⊂GN for Co, Mn, O, and C

(rGO) ($I_D/I_G = 0.98$), which is advantageous for enhancing the electrical conductivity [36]. Benefit from these structures is that the volume expansion can be suppressed during Li$^+$ charge/discharge so as to improve the cycling performance of LIBs [37]. The HRTEM image shows a *d*-spacing value of 0.22 nm, which can be attributed to (200) plane of MnO. The other clear lattice spacings of about 0.25 and 0.16 nm correspond to the (111) and (220) planes of CoMn$_2$O$_4$, respectively. The elemental mapping images of

MnO/CoMn$_2$O$_4$⊂GN are displayed in Fig. 2f. It can be seen that the elements of Co, Mn, and O are highly homogeneously distributed, while C is primarily dispersed outside. This clearly shows that the MnO/CoMn$_2$O$_4$ nanoparticles are incorporated in the rGO layers. The above mapping results are in accordance with EDS spectra of MnO/CoMn$_2$O$_4$⊂GN in Fig. S3b and Table S3.

The crystallographic structure and composition of the MnO/CoMn$_2$O$_4$⊂GN samples are characterized by XRD
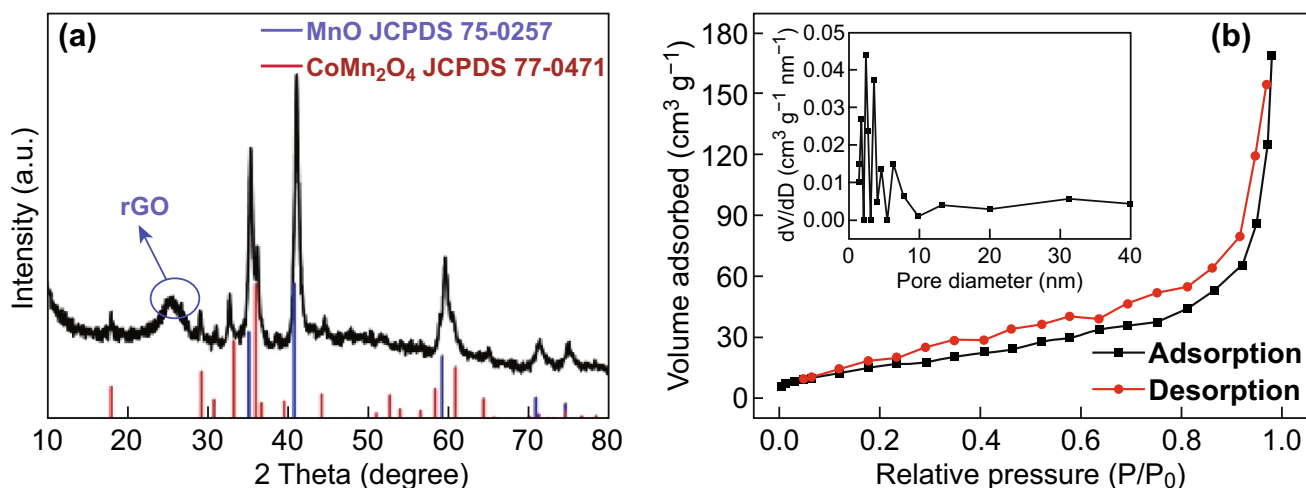
Fig. 3 **a** XRD pattern of the MnO/CoMn$_2$O$_4$⊂GN, **b** Nitrogen adsorption–desorption isotherms and corresponding pore size distribution plot of the MnO/CoMn$_2$O$_4$⊂GN

(Fig. 3a). The weak peak at around 25° assigned to the reduction in GO to rGO, which is marked in Fig. 3a. The spectrum undoubtedly reveals the formation of the CoMn$_2$O$_4$ with a tetragonal crystal structure (JCPDS No. 77-0471) and MnO with a cubic crystal structure (JCPDS No. 75-0257) [38]. In addition, the XRD analysis of pure CoMn$_2$O$_4$ was carried out for comparison and is shown in Fig. S4a. All the dominant diffraction peaks are well matched with the (202), (113), (311), and (404) planes of CoMn$_2$O$_4$ (JCPDS No. 18-0408) [39]. Further, the crystal structure of the sample changes after being coated with graphene sheets. The transformation of the crystallographic structure might be due to the fact that part of the bimetallic oxides is reduced during the hydrothermal process. The specific surface area and pore size of MnO/CoMn$_2$O$_4$⊂GN are calculated by the Brunauer–Emmett–Teller (BET) method and Barrett–Joyner–Halenda (BJH) method, respectively, as shown in Fig. 3b. The MnO/CoMn$_2$O$_4$⊂GN possesses a specific surface area of 136.6 m^2 g^{-1} and an average pore size of 2.7 nm. As compared to MnO/CoMn$_2$O$_4$⊂GN, the BET and BJH methods show that the CoMn$_2$O$_4$ nanoparticles exhibit a smaller specific surface area (31.7 m^2 g^{-1}) and a narrower pore size (2.1 nm), as shown in Fig. S4b.

The chemical composition and electronic properties of the obtained MnO/CoMn$_2$O$_4$⊂GN were further characterized by XPS. It can be found in Fig. 4 that the XPS survey spectrum confirms the existence of Mn, Co, and C elements in the sample. The Mn 2p XPS spectrum (Fig. 4b) contains two main spin–orbit peaks of Mn 2p$_{3/2}$

at 641.8 eV and Mn 2p$_{1/2}$ at 653.5 eV, respectively, corresponding to the presence of both Mn^{2+} and Mn^{3+} [40]. By using a Gaussian fitting method, the Co 2p spectrum (Fig. 4c) is best fitted to two spin–orbit peaks and two shake-up satellites (denoted as sat.). The two major peaks located at 780.7 and 796.4 eV correspond to the Co 2p$_{3/2}$ and Co 2p$_{1/2}$ states with a splitting spin–orbit separation of 15.7 eV, which confirms the presence of Co^{2+} [39]. The XPS spectrum of C 1s (Fig. 4d) consists of three peaks centered at 284.7, 285.9, and 289 eV which can be assigned to C–C, C–O, and O–C=O chemical bands, respectively [41]. According to Fig. S5, when coated with reduced graphene oxides, the contents of C in MnO/CoMn$_2$O$_4$⊂GN increased significantly.

To evaluate the electrochemical performances of the MnO/CoMn$_2$O$_4$⊂GN anode material in LIBs, CV measurements of the MnO/CoMn$_2$O$_4$⊂GN anode were conducted at a voltage range of 0.01–3.0 V versus Li/Li$^+$ with a scan rate of 0.1 mV s^{-1} (Fig. 5a). It is obvious that the CV curve for the first cycle is different from those of the subsequent ones. In the first scan, the peak in the range of 0.1–0.4 V can be attributed to the reduction in MnO/CoMn$_2$O$_4$ to metallic Mn and Co, respectively [42]. The minor broad peak at around 0.75 V can be attributed to the formation of a solid electrolyte interphase (SEI) layer, which is generated by the irreversible decomposition of the solvent in the electrolyte [43]. In the anodic process, two broad peaks at 1.31 and 2.01 V correspond to the oxidation of metallic Mn and Co [44], respectively. In the subsequent cycles, two pairs of
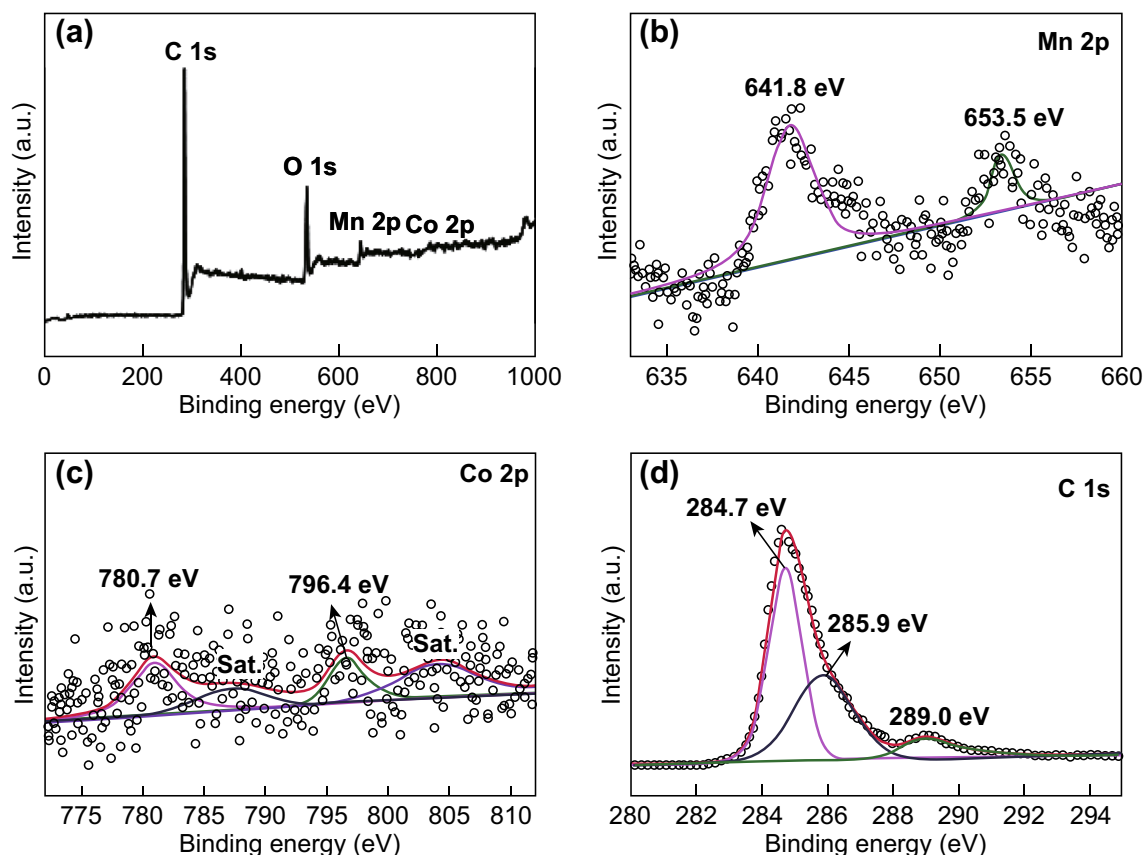
Fig. 4 XPS spectra for the MnO/CoMn$_2$O$_4$⊂GN composites: **a** the survey spectrum and the high-resolution spectra for **b** Mn 2p, **c** Co 2p and **d** C 1s

redox peaks at 0.54/1.38 V and 1.02/2.01 V correspond to the reduction/oxidation in the oxide of Mn and Co, respectively [37]. From the second cycle onward, the CV plots overlap well with each other, demonstrating good reversibility and excellent stability of the MnO/CoMn$_2$O$_4$⊂GN materials [45]. The galvanostatic charge and discharge profiles of MnO/CoMn$_2$O$_4$⊂GN electrode for the first, second, and third cycles at a current density of 0.1 A g^{-1} in the potential range from 0.01 to 3.0 V are shown in Fig. 5b. The MnO/CoMn$_2$O$_4$⊂GN electrode possesses higher initial discharge and charge capacities of 1140 and 735 mAh g^{-1}, respectively, compared to the corresponding theoretical values (921 mAh g^{-1}) [45]. The extra capacity at the first discharge may be due to the formation of the SEI layers [46]. According to calculations, the initial Coulombic efficiency is about 64.5%. The Coulombic efficiency increases as the

cycles growing up and is then continuously maintained around 99%.

The cycling performances of MnO/CoMn$_2$O$_4$⊂GN and pure CoMn$_2$O$_4$ compared at a current density of 0.1 A g^{-1} are shown in Fig. 5c. The specific discharge capacity of MnO/CoMn$_2$O$_4$⊂GN exhibits a slight decrease in the first 24 cycles, followed by a gradual increase to 921 mAh g^{-1} during the 150th cycle. This phenomenon occurs in many transition metal oxides, owing to the high rate lithiation-induced reactivation [47, 48]. The MnO/CoMn$_2$O$_4$⊂GN exhibits a high reversible specific capacity of 921 mAh g^{-1} after 150 cycles, with Coulombic efficiency increased to about 99%. A similar phenomenon can be seen in Fig. 5e and S6 regarding the long-term cycling performance of the MnO/CoMn$_2$O$_4$⊂GN electrode at high current densities of 1 and 5 A g^{-1}. After 1000 cycles, the reversible capacity of MnO/CoMn$_2$O$_4$⊂GN can still remain 622 mAh g^{-1}
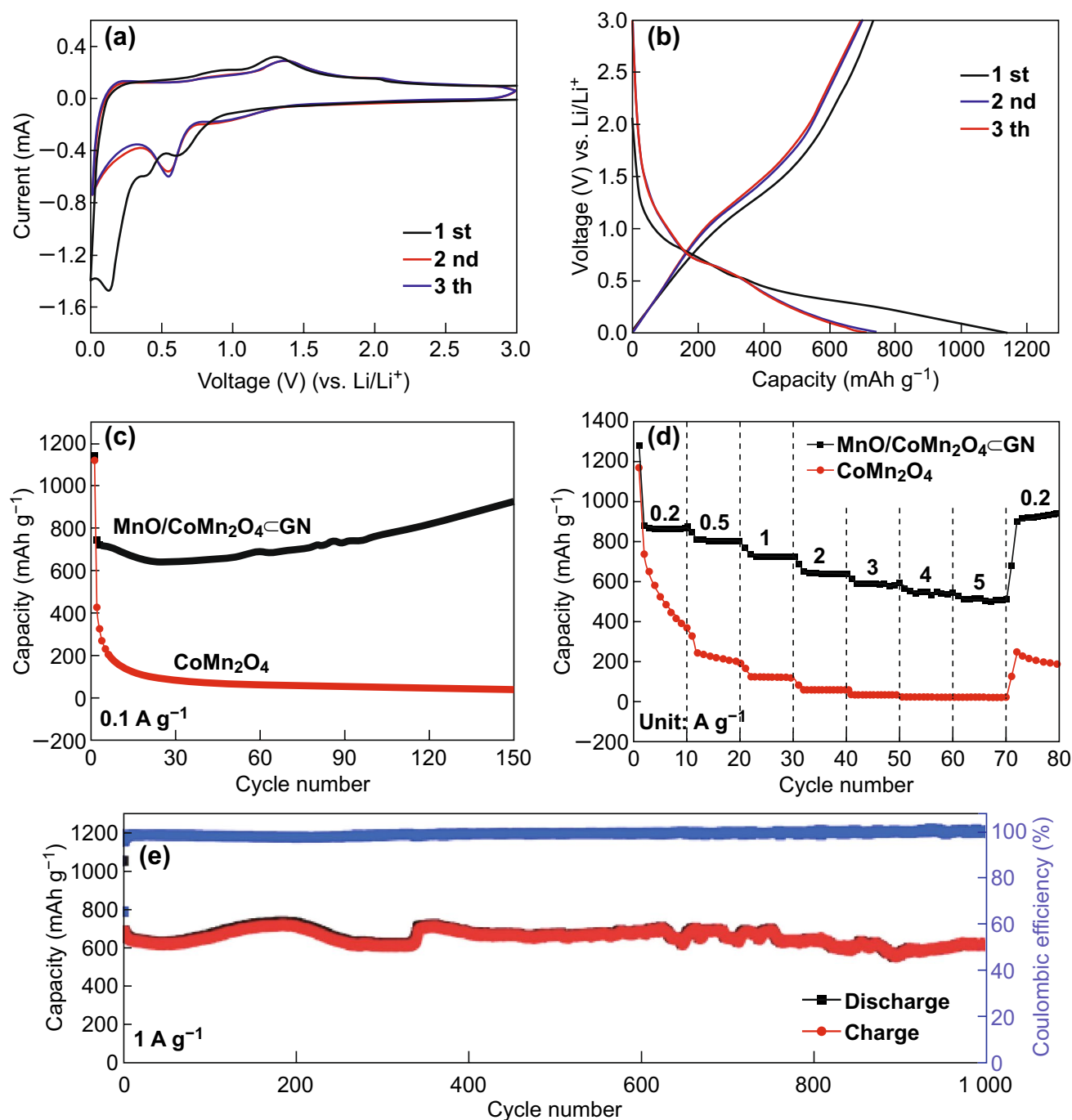
Fig. 5 **a** CV profile of MnO/CoMn$_2$O$_4$⊂GN at a scan rate of 0.1 mV s^{-1} in the voltage range of 0.01–3.0 V. **b** The charge and discharge profiles of MnO/CoMn$_2$O$_4$⊂GN. **c** Cycling performance and Coulombic efficiency of the CoMn$_2$O$_4$ and MnO/CoMn$_2$O$_4$⊂GN electrodes at a current density of 0.1 A g^{-1}. **d** Rate performances of the CoMn$_2$O$_4$ and MnO/CoMn$_2$O$_4$⊂GN electrodes at various current densities. **e** Cycling performance of the MnO/CoMn$_2$O$_4$⊂GN electrode at a current density of 1 A g^{-1}

with its Coulombic efficiency around 100%, confirming the high architectural stability. As a comparison, the cycling performance of pure CoMn$_2$O$_4$ is shown in Fig. S7. Obviously, the CoMn$_2$O$_4$ sample exhibits poor electrochemical properties, delivering a lower initial discharge capacity (1125 mAh g^{-1}) than MnO/CoMn$_2$O$_4$⊂GN, which reduces drastically to 59 mAh g^{-1} after 200 cycles. When increasing or decreasing the content of Mn and GO in Table S1,

the electrochemical performances will all be worse, as can be seen in Fig. S8. The outstanding cycling performance of MnO/CoMn$_2$O$_4$⊂GN might be the result of the unique graphene-coating design. The 3D graphene networks can serve as a conductive matrix to enlarge the interface contact between the active material and electrolyte and shorten the diffusion pathway for lithium ions effectively [41]. In addition, as a compliant buffer, the flexible graphene sheets can accommodate the volume change and prevent the aggregation of MnO/CoMn$_2$O$_4$ nanoparticles during the charge and discharge process [31, 49]. Due to the above reasons, enhanced cycle stability and high reversible capacity can be obtained. In order to further comprehend the electrochemical performance, the rate performances of the CoMn$_2$O$_4$ and MnO/CoMn$_2$O$_4$⊂GN electrodes are also shown in Fig. 5d. It can be seen that the discharge capacities of MnO/CoMn$_2$O$_4$⊂GN are 870.6, 809.6, 731.0, 647.5, 590.4, 545.7, and 515.3 mAh g^{-1} at current densities of 0.2, 0.5, 1, 2, 3, 4, and 5 A g^{-1}, respectively. Moreover, the discharge capacity can deliver up to 914.5 mAh g^{-1} when the current density is back to 0.2 A g^{-1}, revealing remarkable cycling stability and rate capability. In contrast, at current densities of 0.2, 0.5, 1, 2, 3, 4, and 5 A g^{-1}, the capacities of the pure CoMn$_2$O$_4$ are 649.0, 235.7, 127.8, 61.1, 32.5, 21.1, and 20.8 mAh g^{-1}, respectively. Thus, the rate capacity of MnO/CoMn$_2$O$_4$⊂GN is much superior to that of the CoMn$_2$O$_4$. The morphology and structure of the MnO/CoMn$_2$O$_4$⊂GN electrode material after 150 cycles at a current density of 0.1 A g^{-1} are displayed in Fig. S9. In view of the well-preserved surface features, it can be confirmed that MnO/CoMn$_2$O$_4$⊂GN has a stable structure due to the protective effect of the graphene conductive networks.

Electrochemical impedance spectroscopy (EIS) of the CoMn$_2$O$_4$ and MnO/CoMn$_2$O$_4$⊂GN was further investigated as shown in Fig. 6. The MnO/CoMn$_2$O$_4$⊂GN has a smaller diameter of the depressed semicircle at high frequencies compared to the pure CoMn$_2$O$_4$ in the EIS curves. This result clearly explains that the charge transfer resistance of MnO/CoMn$_2$O$_4$⊂GN is smaller during the charge and discharge processes, leading to improved electrode reaction kinetics and better cycling performance.

To further understand the nature of the charge storage process, kinetic study based on CV analysis is carried out. Figure 7a shows the CV measurements of MnO/CoMn$_2$O$_4$⊂GN at different scanning speeds of 0.2, 0.4, 0.6, 0.8, 1.5, and 2 mV s^{-1}. The curves show analogous shapes with three
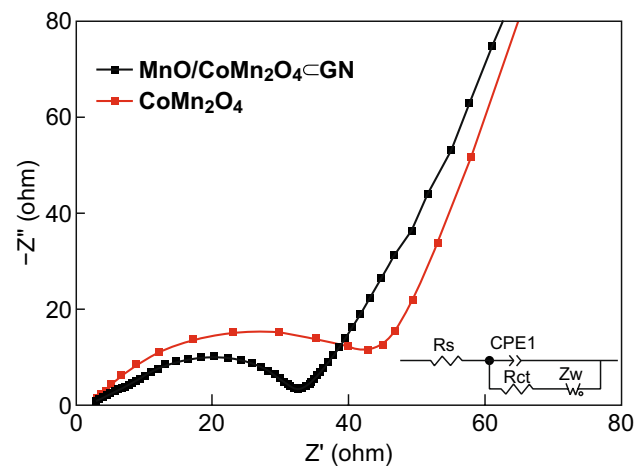
Fig. 6 Electrochemical impedance spectroscopy plots of pure CoMn$_2$O$_4$ and MnO/CoMn$_2$O$_4$⊂GN electrodes

redox peaks during cathodic and anodic processes at each scan rate. It is well known that the capacitance and diffusion-controlled contributions to the whole capacity can be determined by Eqs. 1 and 2 [50]:

$$i = av^b \tag{1}$$

$$\ln i = b \ln v + \ln a \tag{2}$$

where i is the peak current, v is potential sweep rate, a and b are adjustable parameters. The b value is determined by the slope of the $\ln(v) - \ln(i)$ plots according to Eq. 2. When the b value is close to 0.5 or 1.0, the electrochemical system is controlled by ion-diffusion or pseudocapacitance, respectively. From Fig. 7b, the b values for the anodic and cathodic peaks are 0.82, 0.88, and 0.76, implying that the pseudocapacitive behavior primarily controls the electrochemical processes of MnO/CoMn$_2$O$_4$⊂GN electrode, resulting in high rate capabilities [51]. It can be seen that the calculated b values of MnO/CoMn$_2$O$_4$⊂GN are higher than those of pure CoMn$_2$O$_4$ and rGO electrodes in Figs. S10 and S11, suggesting that the pseudocapacitance effect is more significant in MnO/CoMn$_2$O$_4$⊂GN compared to pure CoMn$_2$O$_4$ and rGO. We can use another analysis to further quantify the capacitive contribution to the total lithium storage [52]. The current response i at a certain potential V could be separated into pseudocapacitive effects (k_1v) and diffusion-controlled reactions ($k_2v^{0.5}$), according to Eqs. 3 and 4:

$$i = k_1v + k_2v^{0.5} \tag{3}$$

$$i/v^{0.5} = k_1v^{0.5} + k_2 \tag{4}$$

where the k_1 and k_2 are fixed for the same electrochemical reaction. Figure 7c illustrates the calculated capacitive
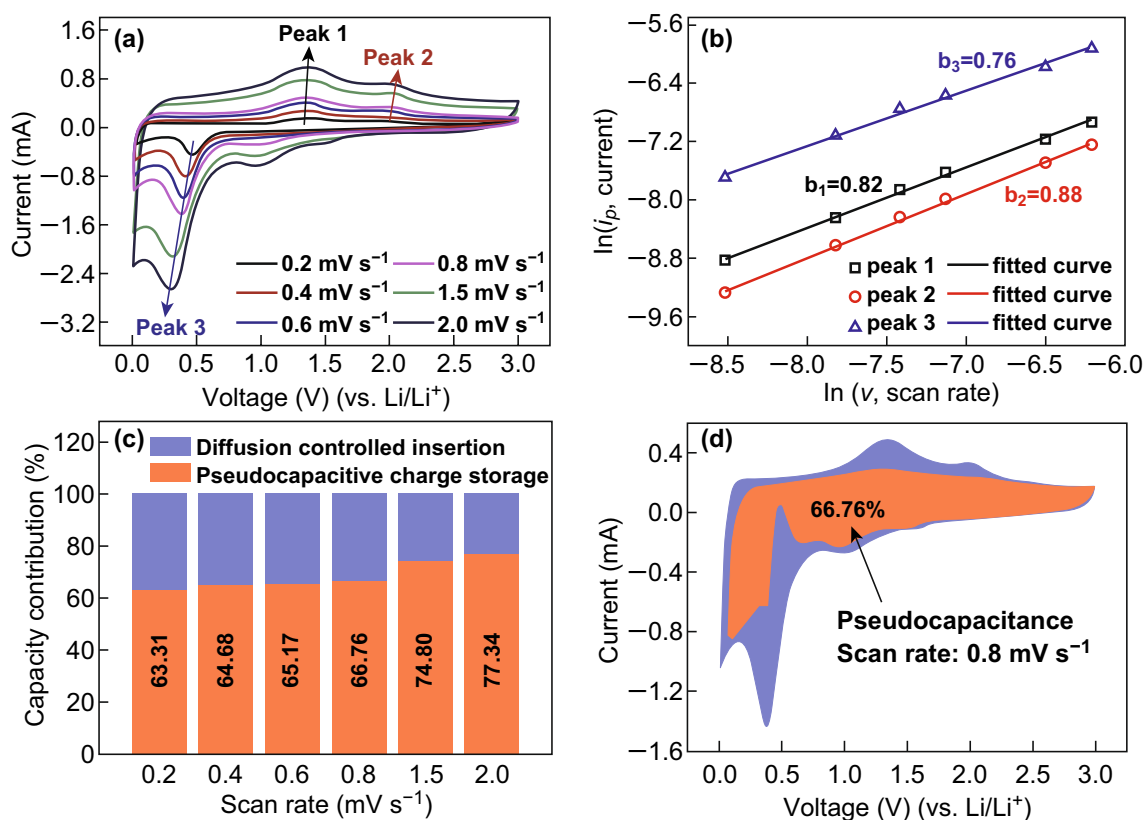
Fig. 7 **a** CV profiles of the $MnO/CoMn_2O_4 \subset GN$ electrodes at different scan rates with the potential range between 0.01 and 3.0 V. **b** The fitted lines and $\ln(i_p)$ versus $\ln(v)$ plots at different oxidation and reduction states. **c** The percentages of pseudocapacitive contribution at different scan rates. **d** Pseudocapacitive (red) and diffusion-controlled (blue) contribution to the charge storage of $MnO/CoMn_2O_4 \subset GN$ at 0.8 mV s^{-1}. (Color figure online)

contribution at various scan rates. It can be found that the percentage of capacitive contribution keeps increasing with increase in the scan rate from 0.2 to 2 mV s^{-1}, which well explains the superior rate capability. The typical voltage profile for the dominating capacitive contributions (red region) in comparison with the whole area is shown in Fig. 7d. At a scan rate of 0.8 mV s^{-1}, the pseudocapacitive contribution is calculated to be 66.76%, suggesting that the capacity contribution is dominated by pseudocapacitance. It can be observed that the capacitive capacity keeps increasing along with the increase in voltage scan rates, and pseudocapacitive contribution is more dominant in the total capacity for $MnO/CoMn_2O_4 \subset GN$ compared to pure $CoMn_2O_4$ and rGO.

To highlight the electrochemical performances of the $MnO/CoMn_2O_4 \subset GN$ in this work, other similar electrode materials reported in the previous literature are also compared and presented in Fig. 8. According to the line chart, the as-prepared $MnO/CoMn_2O_4 \subset GN$ electrode can deliver a higher current density when comparing with other similar anode materials reported in recent studies like Co_3O_4

nanocrystals [48], $CoMn_2O_4$ hollow nanofibers [39], $MnCo_2O_4$ hollow microspheres [45], porous $MnCo_2O_4$ microspheres [47], hierarchical hollow structured $CoMn_2O_4$ microflowers [53], single-crystalline $CoMn_2O_4$ nano/submicrorods [54], Fe_2O_3 nanotubes@Co_3O_4 composite particles [55], and $ZnCo_2O_4$ nanocluster particles [56], indicating that the unique architecture of bimetallic oxides nanoparticles encapsulated in 3D graphene networks can largely enhance the electrochemical performance of anode materials.

As mentioned above, the pure $CoMn_2O_4$ nanoparticles can be synthesized via metal–oleate decomposition method rapidly and on a large scale. The synthetic procedure is a general approach to synthesize different kinds of transition metal oxides. The porous $MnO/CoMn_2O_4 \subset GN$ is fabricated by coating the $MnO/CoMn_2O_4$ with rGO through a self-assembly process. As an anode material for LIBs, the $MnO/CoMn_2O_4 \subset GN$ displays superior and excellent electrochemical performances which could be attributed to the following factors. Firstly, the unique
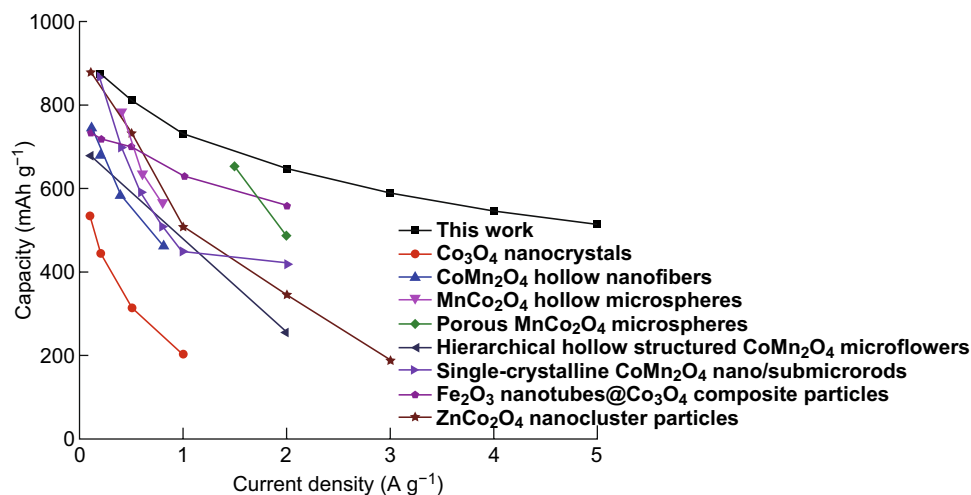
Fig. 8 Comparison of the lithium storage properties of the MnO/CoMn$_2$O$_4$ $\subset$ GN to similar anode materials reported in other studies

porous architecture promotes the charge transfer so as to enhance the reversible capacity by shortening the diffusion length of the lithium ion [57]. Secondly, the presence of 3D graphene networks can not only facilitate the transport of lithium ions and electrons but also buffer the large volume change of anodes and alleviate the pulverization problem, leading to excellent cyclic stability. Furthermore, the synergetic effect between the 0D nanoparticles and 3D graphene networks plays an essential role in the superb electrochemical performances of MnO/CoMn$_2$O$_4$ $\subset$ GN electrode. The void space in the MnO/CoMn$_2$O$_4$ $\subset$ GN can facilitate electron and ion transportation. The 3D graphene networks can also improve the electrical conductivity and help to increase the mechanical strength, leading to superior electrochemical performance, such as high specific capacity, outstanding cycle stability, and excellent rate capability.

4 Conclusions

In summary, we synthesize a novel architecture consisting of 0D nanoparticles encapsulated in 3D interconnected graphene networks by a self-assembly route. When used as an anode for LIBs, the unique MnO/CoMn$_2$O$_4$ $\subset$ GN nanocomposites hold several structural and compositional advantages including improved electrical conductivity, reduced diffusion length for Li$^+$ ions, minimized volume variation, and increased number of active sites for electrochemical reactions. The MnO/CoMn$_2$O$_4$ $\subset$ GN anode exhibits a pseudocapacitance-boosted ultrafast lithium storage performance in terms of high capacity and good cycling stability (921 mAh g^{-1} over 150 cycles at 0.1 A g^{-1}), as well as outstanding rate capability (about 515 mAh g^{-1} at 5 A g^{-1}). This study may inspire the design and construction of advanced anode materials for LIBs.

Electronic supplementary material The online version of this article (https://doi.org/10.1007/s40820-019-0247-3) contains supplementary material, which is available to authorized users.

References

1. K. Kang, Y.S. Meng, J. Bréger, C.P. Grey, G. Ceder, Electrodes with high power and high capacity for rechargeable lithium batteries. Science **311**(5763), 977–980 (2006). https://doi.org/10.1126/science.1122152

2. J. Wang, N. Yang, H. Tang, Z. Dong, Q. Jin et al., Accurate control of multishelled Co_3O_4 hollow microspheres as high-performance anode materials in lithium-ion batteries. Angew. Chem. Int. Ed. **52**(25), 6417–6420 (2013). https://doi.org/10.1002/anie.201301622

3. B. Li, N. Jiang, W. Huang, H. Yan, Y. Zuo, D. Xia, Thermodynamic activation of charge transfer in anionic redox process for Li-ion batteries. Adv. Funct. Mater. **28**(4), 1704864 (2018). https://doi.org/10.1002/adfm.201704864

4. L. Zhou, D. Zhao, X. Lou, $LiNi_{0.5}Mn_{1.5}O_4$ hollow structures as high-performance cathodes for lithium-ion batteries. Angew. Chem. Int. Ed. **51**, 239–241 (2012). https://doi.org/10.1002/anie.201106998

5. Z. Liu, L. Feng, X. Su, C. Qin, K. Zhao, F. Hu, M. Zhou, Y. Xia, Micro-sized organometallic compound of ferrocene as high-performance anode material for advanced lithium-ion batteries. J. Power Sources **375**, 102–105 (2018). https://doi.org/10.1016/j.jpowsour.2017.11.064

6. X. Zhou, L.J. Wan, Y.G. Guo, Binding SnO_2 nanocrystals in nitrogen-doped graphene sheets as anode materials for lithium-ion batteries. Adv. Mater. **25**(15), 2152–2157 (2013). https://doi.org/10.1002/adma.201300071

7. H. Liu, W. Zhao, R. Li, X. Huang, Y. Tang, D. Li, F. Huang, Facile synthesis of reduced graphene oxide in situ wrapped $MnTiO_3$ nanoparticles for excellent lithium storage. J. Inorg. Mater. **33**(9), 1022–1028 (2018). https://doi.org/10.15541/jim20180143

8. Z. Luo, J.C. Xu, B. Yuan, H. Li, R.Z. Hu, L.C. Yang, Y. Gao, M. Zhu, A novel 3D bimodal porous current collector with large interconnected spherical channels for improved capacity and cycling stability of Sn anode in Li-ion batteries. Mater. Lett. **213**, 189–192 (2018). https://doi.org/10.1016/j.matlett.2017.11.089

9. H. Shang, Z. Zuo, L. Li, F. Wang, H. Liu, Y. Li, Y. Li, Ultrathin graphdiyne nanosheets grown in situ on copper nanowires and their performance as lithium-ion battery anodes. Angew. Chem. Int. Ed. **57**(3), 774–778 (2018). https://doi.org/10.1002/anie.201711366

10. L. Qie, W.M. Chen, Z.H. Wang, Q.G. Shao, X. Li et al., Nitrogen-doped porous carbon nanofiber webs as anodes for lithium ion batteries with a superhigh capacity and rate capability. Adv. Mater. **24**(15), 2047–2050 (2012). https://doi.org/10.1002/adma.201104634

11. P. Poizot, S. Laruelle, S. Grugeon, L. Dupont, J.M. Tarascon, Nano-sized transition-metal oxides as negative-electrode materials for lithium-ion batteries. Nature **407**, 496–499 (2000). https://doi.org/10.1038/35035045

12. Y. Jiang, Z.-J. Jiang, L. Yang, S. Cheng, M. Liu, A high-performance anode for lithium ion batteries: Fe_3O_4 microspheres encapsulated in hollow graphene shells. J. Mater. Chem. A **3**(22), 11847–11856 (2015). https://doi.org/10.1039/c5ta01848j

13. D. Xu, C. Mu, J. Xiang, F. Wen, C. Su, C. Hao, W. Hu, Y. Tang, Z. Liu, Carbon-encapsulated Co_3O_4@CoO@Co nanocomposites for multifunctional applications in enhanced long-life lithium storage, supercapacitor and oxygen evolution reaction. Electrochim. Acta **220**, 322–330 (2016). https://doi.org/10.1016/j.electacta.2016.10.116

14. L. Wang, Y. Fu, Y. Chen, Y. Li, R. Zhou, S. Chen, Y. Song, Ultralight flower ball-like Co_3O_4/melamine-derived carbon foam as anode materials for lithium-ion batteries. J. Alloys Compd. **724**, 1117–1123 (2017). https://doi.org/10.1016/j.jallcom.2017.07.130

15. J. Mujtaba, H. Sun, Y. Zhao, G. Xiang, S. Xu, J. Zhu, High-performance lithium storage based on the synergy of atomic-thickness nanosheets of TiO_2 (B) and ultrafine Co_3O_4 nanoparticles. J. Power Sources **363**, 110–116 (2017). https://doi.org/10.1016/j.jpowsour.2017.07.076

16. L. Wang, Y. Zheng, X. Wang, S. Chen, F. Xu et al., Nitrogen-doped porous carbon/Co_3O_4 nanocomposites as anode materials for lithium-ion batteries. ACS Appl. Mater. Interfaces **6**(10), 7117–7125 (2014). https://doi.org/10.1021/am406053s

17. H. Sun, H. Liu, Y. Yu, M. Ahmad, D. Nan, J. Zhu, Mesoporous Co_3O_4 nanosheets-3D graphene networks hybrid materials for high-performance lithium ion batteries. Electrochim. Acta **118**, 1–9 (2014). https://doi.org/10.1016/j.electacta.2013.11.181

18. Z. Cui, S. Wang, Y. Zhang, M. Cao, High-performance lithium storage of Co_3O_4 achieved by constructing porous nanotube structure. Electrochim. Acta **182**, 507–515 (2015). https://doi.org/10.1016/j.electacta.2015.09.120

19. G.Y. Huang, S.M. Xu, Y. Yang, Y.B. Cheng, J. Li, Preparation of cobalt-based Bi-metal-oxides and the application in the field of electrochemical energy storage. Chin. J. Inorg. Chem. **32**(10), 1693–1703 (2016). https://doi.org/10.11862/CJIC.2016.244

20. F. Zheng, G. Xia, Y. Yang, Q. Chen, MOF-derived ultrafine MnO nanocrystals embedded in a porous carbon matrix as high-performance anodes for lithium-ion batteries. Nanoscale **7**(21), 9637–9645 (2015). https://doi.org/10.1039/c5nr00528k

21. P. Rosaiah, J. Zhu, O.M. Hussain, Y. Qiu, Graphenothermal reduction synthesis of MnO/RGO composite with excellent anodic behaviour in lithium ion batteries. Ceram. Int. **44**(3), 3077–3084 (2018). https://doi.org/10.1016/j.ceramint.2017.11.070

22. Y. Deng, L. Wan, Y. Xie, X. Qin, G. Chen, Recent advances in Mn-based oxides as anode materials for lithium ion batteries. RSC Adv. **4**(45), 23914–23935 (2014). https://doi.org/10.1039/c4ra02686a

23. H. Jiang, Y. Hu, S. Guo, C. Yan, P.S. Lee, C. Li, Rational design of MnO/carbon nanopeapods with internal void space for high-rate and long-life Li-ion batteries. ACS Nano **8**(6), 6038–6046 (2014). https://doi.org/10.1021/nn501310n

24. X. Liu, C. Chen, Y. Zhao, B. Jia, A review on the synthesis of manganese oxide nanomaterials and their applications on

lithium-ion batteries. J. Nanomater. **2013**, 1–7 (2013). https://doi.org/10.1155/2013/736375

25. J. Zhou, S. Cheng, Y. Jiang, F. Zheng, X. Ou et al., Fabrication of TiO_2 coated porous $CoMn_2O_4$ submicrospheres for advanced lithium-ion anodes. RSC Adv. **7**(34), 21214–21220 (2017). https://doi.org/10.1039/c7ra02789c

26. Y. Zhang, X. Wang, Q. Zhao, Y. Fu, H. Wang, H. Shu, Facile preparation and performance of hierarchical self-assembly $MnCo_2O_4$ nanoflakes as anode active material for lithium ion batteries. Electrochim. Acta **180**, 866–872 (2015). https://doi.org/10.1016/j.electacta.2015.09.037

27. J. Bai, X. Li, G. Liu, Y. Qian, S. Xiong, Unusual formation of $ZnCo_2O_4$ 3D hierarchical twin microspheres as a high-rate and ultralong-life lithium-ion battery anode material. Adv. Funct. Mater. **24**(20), 3012–3020 (2014). https://doi.org/10.1002/adfm.201303442

28. L. Yao, X. Hou, S. Hu, J. Wang, M. Li et al., Green synthesis of mesoporous $ZnFe_2O_4$/C composite microspheres as superior anode materials for lithium-ion batteries. J. Power Sources **258**, 305–313 (2014). https://doi.org/10.1016/j.jpowsour.2014.02.055

29. M. Khan, M.N. Tahir, S.F. Adil, H.U. Khan, M.R.H. Siddiqui, A.A. Al-warthan, W. Tremel, Graphene based metal and metal oxide nanocomposites: synthesis, properties and their applications. J. Mater. Chem. A **3**(37), 18753–18808 (2015). https://doi.org/10.1039/c5ta02240a

30. S. Park, R.S. Ruoff, Chemical methods for the production of graphenes. Nat. Nanotechnol. **4**(4), 217–224 (2009). https://doi.org/10.1038/nnano.2009.58

31. G. Gao, S. Lu, Y. Xiang, B. Dong, W. Yan, S. Ding, Free-standing ultrathin $CoMn_2O_4$ nanosheets anchored on reduced graphene oxide for high-performance supercapacitors. Dalton Trans. **44**(43), 18737–18742 (2015). https://doi.org/10.1039/c5dt03696h

32. X. Yang, K. Fan, Y. Zhu, J. Shen, X. Jiang, P. Zhao, S. Luan, C. Li, Electric papers of graphene-coated Co_3O_4 fibers for high-performance lithium-ion batteries. ACS Appl. Mater. Interfaces **5**(3), 997–1002 (2013). https://doi.org/10.1021/am302685t

33. H. Wang, L.-F. Cui, Y. Yang, H. Sanchez Casalongue, J.T. Robinson, Y. Liang, Y. Cui, H. Dai, Mn_3O_4-graphene hybrid as a high-capacity anode material for lithium ion batteries. J. Am. Chem. Soc. **132**(40), 13978–13980 (2010). https://doi.org/10.1021/ja105296a

34. P. Jie, G. Hongbo, A. Huixiang, Z. Lingling, W. Huaixin, C. Xueqin, Z. Junwei, G. Hongwei, Three-dimensional nitrogen and sulfur Co-doped holey-reduced graphene oxide frameworks anchored with MoO_2 nanodots for advanced rechargeable lithium-ion batteries. Nanotechnology **29**(29), 295404 (2018). https://doi.org/10.1088/1361-6528/aac02c

35. C. Chen, J. Xi, E. Zhou, L. Peng, Z. Chen, C. Gao, Porous graphene microflowers for high-performance microwave absorption. Nano-Micro Lett. **10**(2), 26 (2018). https://doi.org/10.1007/s40820-017-0179-8

36. D. Gu, Y. Zhou, R. Ma, F. Wang, Q. Liu, J. Wang, Facile synthesis of N-doped graphene-like carbon nanoflakes as

efficient and stable electrocatalysts for the oxygen reduction reaction. Nano-Micro Lett. **10**(2), 29 (2018). https://doi.org/10.1007/s40820-017-0181-1

37. L. Zhou, D. Zhao, X.W. Lou, Double-shelled $CoMn_2O_4$ hollow microcubes as high-capacity anodes for lithium-ion batteries. Adv. Mater. **24**(6), 745–748 (2012). https://doi.org/10.1002/adma.201104407

38. A. Jha, D. Mhamane, A. Suryawanshi, S.M. Joshi, P. Shaikh, N. Biradar, S. Ogale, C.V. Rode, Triple nanocomposites of $CoMn_2O_4$, Co_3O_4 and reduced graphene oxide for oxidation of aromatic alcohols. Catal. Sci. Technol. **4**(6), 1771–1778 (2014). https://doi.org/10.1039/c3cy01025b

39. G. Yang, X. Xu, W. Yan, H. Yang, S. Ding, Single-spinneret electrospinning fabrication of $CoMn_2O_4$ hollow nanofibers with excellent performance in lithium-ion batteries. Electrochim. Acta **137**, 462–469 (2014). https://doi.org/10.1016/j.electacta.2014.05.167

40. Y. Xu, X. Wang, C. An, Y. Wang, L. Jiao, H. Yuan, Facile synthesis route of porous $MnCo_2O_4$ and $CoMn_2O_4$ nanowires and their excellent electrochemical properties in supercapacitors. J. Mater. Chem. A **2**(39), 16480–16488 (2014). https://doi.org/10.1039/c4ta03123g

41. G. Qu, H. Geng, D. Ge, J. Zheng, H. Gu, Graphene-coated mesoporous Co_3O_4 fibers as an efficient anode material for Li-ion batteries. RSC Adv. **6**(75), 71006–71011 (2016). https://doi.org/10.1039/c6ra15404b

42. Y. Li, X. Hou, Y. Li, Q. Ru, S. Wang, S. Hu, K.-H. Lam, Facile synthesis of hierarchical $CoMn_2O_4$ microspheres with porous and micro-/nanostructural morphology as anode electrodes for lithium-ion batteries. Electron. Mater. Lett. **13**(5), 427–433 (2017). https://doi.org/10.1007/s13391-017-6258-7

43. M. Bijelić, X. Liu, Q. Sun, A.B. Djurišić, M.H. Xie et al., Long cycle life of $CoMn_2O_4$ lithium ion battery anodes with high crystallinity. J. Mater. Chem. A **3**(28), 14759–14767 (2015). https://doi.org/10.1039/c5ta03570h

44. M.H. Kim, Y.J. Hong, Y.C. Kang, Electrochemical properties of yolk-shell and hollow $CoMn_2O_4$ powders directly prepared by continuous spray pyrolysis as negative electrode materials for lithium ion batteries. RSC Adv. **3**(32), 13110–13114 (2013). https://doi.org/10.1039/c3ra41314d

45. J. Li, S. Xiong, X. Li, Y. Qian, A facile route to synthesize multiporous $MnCo_2O_4$ and $CoMn_2O_4$ spinel quasi-hollow spheres with improved lithium storage properties. Nanoscale **5**(5), 2045–2054 (2013). https://doi.org/10.1039/c2nr33576j

46. Y. Sharma, N. Sharma, G.V.S. Rao, B.V.R. Chowdari, Li-storage and cyclability of urea combustion derived $ZnFe_2O_4$ as anode for Li-ion batteries. Electrochim. Acta **53**(5), 2380–2385 (2008). https://doi.org/10.1016/j.electacta.2007.09.059

47. G. Li, L. Xu, Y. Zhai, Y. Hou, Fabrication of hierarchical porous $MnCo_2O_4$ and $CoMn_2O_4$ microspheres composed of polyhedral nanoparticles as promising anodes for long-life LIBs. J. Mater. Chem. A **3**(27), 14298–14306 (2015). https://doi.org/10.1039/c5ta03145a

48. D. Ge, J. Wu, G. Qu, Y. Deng, H. Geng, J. Zheng, Y. Pan, H. Gu, Rapid and large-scale synthesis of bare Co_3O_4 porous nanostructures from an oleate precursor as superior Li-ion

anodes with long-cycle lives. Dalton Trans. **45**(34), 13509–13513 (2016). https://doi.org/10.1039/c6dt02136k

49. D. Cai, B. Qu, Q. Li, H. Zhan, T. Wang, Reduced graphene oxide uniformly anchored with ultrafine $CoMn_2O_4$ nanoparticles as advance anode materials for lithium and sodium storage. J. Alloys Compd. **716**, 30–36 (2017). https://doi.org/10.1016/j.jallcom.2017.05.023

50. C. Yang, Y. Zhang, F. Lv, C. Lin, Y. Liu et al., Porous $ZrNb_{24}O_{62}$ nanowires with pseudocapacitive behavior achieve high-performance lithium-ion storage. J. Mater. Chem. A **5**(42), 22297–22304 (2017). https://doi.org/10.1039/C7TA07347J

51. B.H. Hou, Y.Y. Wang, J.Z. Guo, Q.L. Ning, X.T. Xi et al., Pseudocapacitance-boosted ultrafast Na storage in a pie-like FeS@C nanohybrid as an advanced anode material for sodium-ion full batteries. Nanoscale **10**(19), 9218–9225 (2018). https://doi.org/10.1039/c7nr09674g

52. X. Deng, Z. Wei, C. Cui, Q. Liu, C. Wang, J. Ma, Oxygen-deficient anatase TiO_2@C nanospindles with pseudocapacitive contribution for enhancing lithium storage. J. Mater. Chem. A **6**(9), 4013–4022 (2018). https://doi.org/10.1039/C7TA11301C

53. L. Zhang, G. He, S. Lei, G. Qi, H. Jiu, J. Wang, Hierarchical hollow microflowers constructed from mesoporous single crystalline $CoMn_2O_4$ nanosheets for high performance anode of lithium ion battery. J. Power Sources **326**, 505–513 (2016). https://doi.org/10.1016/j.jpowsour.2016.07.021

54. L. Wang, B. Liu, S. Ran, L. Wang, L. Gao, F. Qu, D. Chen, G. Shen, Facile synthesis and electrochemical properties of $CoMn_2O_4$ anodes for high capacity lithium-ion batteries. J. Mater. Chem. A **1**(6), 2139–2143 (2013). https://doi.org/10.1039/c2ta00125j

55. S.L. Zhang, B.Y. Guan, H.B. Wu, X.W.D. Lou, Metal-organic framework-assisted synthesis of compact Fe_2O_3 nanotubes in Co_3O_4 host with enhanced lithium storage properties. Nano-Micro Lett. **10**(3), 44 (2018). https://doi.org/10.1007/s40820-018-0197-1

56. Y. Pan, W. Zeng, L. Li, Y. Zhang, Y. Dong, A facile synthesis of $ZnCo_2O_4$ nanocluster particles and the performance as anode materials for lithium ion batteries. Nano-Micro Lett. **9**(2), 20 (2017). https://doi.org/10.1007/s40820-016-0122-4

57. L. Yao, J. Wu, H. Deng, Q.-A. Huang, Q. Su, G. Du, $MnCo_2O_4$/graphene composites anchored on Ni foam as binder-free anode with enhanced lithium-storage performance. Mater. Lett. **180**, 188–191 (2016). https://doi.org/10.1016/j.matlet.2016.05.177